

Effects of viscoelasticity on drop impact and spreading on a solid surface

Daulet Izbassarov and Metin Muradoglu^{*}

Department of Mechanical Engineering, Koç University, Rumelifeneri Yolu, 34450 Sarıyer, İstanbul, Turkey

(Received 3 February 2016; published 10 June 2016)

The effects of viscoelasticity on drop impact and spreading on a flat solid surface are studied computationally using a finite-difference-front-tracking method. The finitely extensible nonlinear elastic–Chilcott–Rallison model is used to account for the fluid viscoelasticity. It is found that viscoelasticity favors advancement of contact line during the spreading phase, leading to a slight increase in the maximum spreading, in agreement with experimental observations [Huh, Jung, Seo, and Lee, *Microfluid. Nanofluid.* **18**, 1221 (2015)]. However, in contrast with the well-known antirebound effects of polymeric additives, the viscoelasticity is found to enhance the tendency of the drop rebound in the receding phase. These results suggest that the antirebound effects are mainly due to the polymer-induced modification of wetting properties of the substrate rather than the change in the material properties of the drop fluid. A model is proposed to test this hypothesis. It is found that the model results in good qualitative agreement with the experimental observations and the antirebound behavior can be captured by the modification of surface wetting properties in the receding phase.

DOI: [10.1103/PhysRevFluids.1.023302](https://doi.org/10.1103/PhysRevFluids.1.023302)

I. INTRODUCTION

Controlled deposition of a droplet on a flat substrate is an important problem in many applications including pesticide deposition [1], spray coating [2], inkjet printing [3], additive manufacturing [4], tissue engineering, and single-cell epitaxy [5,6]. It is particularly important to know whether a droplet will deposit or rebound after the impact. In the literature, a Newtonian droplet impacting on a flat substrate has been extensively investigated [4,7]. The influence of viscoelasticity on the impact and spreading of a droplet on a substrate has received growing attention in recent years particularly due to the discovery of the antirebound effects of polymer additives [1,8].

Unlike the Newtonian systems, understanding of the impact dynamics of a viscoelastic droplet is severely limited and yet of great importance for a wide range of applications. It has been reported that a tiny amount of polymer such as polyethylene oxide added to water can dramatically affect drop dynamics, suppressing the rebounding of a drop on a hydrophobic substrate. Based on experimental observations, several hypotheses have been proposed to explain this interesting behavior, which often led to controversies. Initially, the antirebound effect was thought to be due to large energy dissipation caused by the elongational viscosity of the polymers [1]. However, further studies have detected some flaws in this hypothesis. Bertola [9] and Rozhkov *et al.* [10] examined the influence of the substrate on the retraction of polymeric drops using a hot surface (Leidenfrost drops) and small targets, respectively. They both found that the polymer additives do not change the retraction velocity significantly and thus concluded that the antirebound effect cannot be explained by the elongational viscosity of the fluid. Bartolo *et al.* [11] proposed an alternative hypothesis based on their own experimental observations and suggested that the polymer additives generate high normal stresses near the moving contact line of the drop that counter the capillary force and in turn prevent rebound of the drop. However, Bertola [8] has recently raised questions about this hypothesis. Bartolo *et al.* [11] explained the antirebound phenomenon observed in dilute solutions using the values of the normal stresses measured in semidilute solutions, which are orders of magnitude different. Thus

*Corresponding author: mmuradoglu@ku.edu.tr

the slow retraction might be mainly caused by high shear viscosity rather than the normal stresses. In addition, according to their own rheometrical data [11], the dilute polymer solutions do not exhibit appreciable normal stresses in the range of shear rates that occur during the receding phase. Recent experimental studies have provided evidence that the antirebound effect might be due to the modification of dynamic wetting properties by the polymers deposited on the substrate rather than the change in the bulk fluid properties. Smith and Bertola [12] observed that polymer molecules that are left behind the contact line produce a resistant force during the retraction and act to prevent a drop from rebounding. Zang *et al.* [13] investigated impact dynamics of droplets containing nanoparticles and polymers. They concluded that drop rebound is inhibited by enhanced friction due to interaction of particles and polymers with the substrate. Later, Zang *et al.* [14] demonstrated that the rebounding of a viscoelastic droplet can be restored via nanoparticle enwrapping and thus concluded that the antirebound effect is related to the drop-substrate friction rather than the bulk rheological properties. Smith and Sharp [15] provided further evidence that polymers deposited on the substrate result in a velocity-dependent friction force at the contact line during the droplet retraction phase. Bertola and Wang [16] have also confirmed the existence of the polymer-induced friction and showed that the receding contact angle in polymer solution drops is significantly smaller than that in the pure water drops. They also observed that the minimum contact angle decreases with respect to both increasing polymer concentration and the Weber number. Biolè and Bertola [17] provided significant experimental evidence that the main contribution to the contact line friction is given by small liquid filaments pulling the contact line in the radial direction. In addition, Huh *et al.* [18] have shown that energy dissipation is significantly increased during the retraction phase due to polymeric residues left on the substrate. They found that the energy dissipation increases with the molecular weight and concentration of the polymer. Based on these experimental findings, they proposed a semiempirical model to estimate the rebounding tendency of a polymer solution drop. The impact and spreading of polymeric drops on solid surfaces have been recently reviewed by Bertola [8].

On the computational side, various numerical techniques have been used to model a viscoelastic drop impacting on a solid surface. The smoothed particle hydrodynamics (SPH) method has been used by several groups for this purpose, including Fang *et al.* [19] and Jiang *et al.* [20–22]. In these studies, the effects of surface tension have been ignored and the main focus has been placed on the numerical method rather than examination of flow physics. Fang *et al.* [19] simulated impact of an Oldroyd-B fluid droplet on a rigid plate using a SPH method. They found that the viscoelasticity enhances both spreading and contraction. Jiang *et al.* [20] studied impact and spreading of an Oldroyd-B fluid droplet on an inclined surface. They found that the viscoelastic droplet spreads faster than the Newtonian counterpart. Jiang *et al.* [21] simulated the impact of a highly viscous extended Pom-Pom (XPP) fluid droplet at high Weissenberg numbers. They found that the viscoelasticity increases spreading but decreases the tendency to contraction. Jiang *et al.* [22] investigated the spreading process of two XPP model droplets impacting on a plate in a sequence at a low Reynolds number. Their results revealed that model parameters have significant influence on the deformation process of the XPP droplets. They also confirmed the enhancement of drop spreading with the Weissenberg number. Grid-based methods have also been used to study the drop impact problem. For instance, Tomé *et al.* [23], Oishi *et al.* [24], and Paulo *et al.* [25] have investigated a viscoelastic drop impacting on a flat solid substrate using a marker-and-cell method with various viscoelastic models including the Oldroyd-B [23], XPP [24], and finitely extensible nonlinear elastic–Chilcott–Rallison (FENE-CR) [25] models. The problem has been simplified by assuming a nonwetting substrate and neglecting the effects of the surface tension. In addition, these works have all assumed a planar two-dimensional configuration. Tomé *et al.* [23] simulated impact of an Oldroyd-B drop on a rigid plate and found that a viscoelastic droplet exhibits a greater tendency for spreading compared to the Newtonian one. They also found that only the viscoelastic droplet undergoes a significant contraction. Oishi *et al.* [24] studied the XPP drop impact problem for a wide range of flow conditions. They found that the drop spreading increases with increasing Weissenberg number and decreasing solvent viscosity ratio. Paulo *et al.* [25] simulated impact of a FENE-CR droplet and reported that the viscoelasticity favors drop spreading. More recently, Wang *et al.* [26] have investigated the dynamic

wetting of viscoelastic droplets on a solid substrate using a phase-field method. They ignored the inertial effects but accounted for the surface tension. They also found that the viscoelastic droplets spread faster than the Newtonian counterparts.

In this paper we computationally study the effects of viscoelasticity on drop impact, spreading, and rebound on a solid surface. We fully account for the effects of surface tension and treat the partial wetting cases with a dynamic contact angle. The Navier-Stokes and the viscoelastic model equations are solved in the entire computational domain using a front-tracking method [27–29]. The fluid viscoelasticity is characterized by the Weissenberg number Wi , the concentration parameter defined as the ratio of polymeric viscosity to solvent viscosity c , and the extensibility parameter L . We first examine the effects of drop viscoelasticity without the polymer-induced contact angle hysteresis and find that the drop viscoelasticity enhances the rebounding tendency, which is in contrast with the experimental observations. To remedy this deficiency, we propose a model that mimics the hysteresis of the contact angle observed experimentally by Bertola and Wang [16]. The simulations with the contact line hysteresis result in good qualitative agreement with the experimental observations [16], supporting the hypothesis that the antirebound effect is mainly due to the modification of surface wetting properties by the deposited polymer molecules rather than the drop viscoelasticity. Although the emphasis is placed on the effects of the viscoelasticity, further simulations are also carried out to examine the effects of the Weber number We , the Reynolds number Re , and the equilibrium contact angle θ_e .

II. FORMULATION AND NUMERICAL METHOD

The governing equations are described in the framework of the finite-difference–front-tracking method. The flow is assumed to be incompressible. Following Unverdi and Tryggvason [27] and Izbassarov and Muradoglu [29,30], a single set of governing equations can be written for the entire computational domain provided the jumps in the material properties such as density, viscosity, and relaxation time are taken into account and the effects of the interfacial surface tension are treated appropriately. In this approach, the mass and momentum conservation equations can be written as

$$\nabla \cdot \mathbf{u} = 0, \quad (1)$$

$$\frac{\partial \rho \mathbf{u}}{\partial t} + \nabla \cdot (\rho \mathbf{u} \mathbf{u}) = -\nabla p + \nabla \cdot \mu_s (\nabla \mathbf{u} + \nabla \mathbf{u}^T) + \nabla \cdot \boldsymbol{\sigma} + \int_A \gamma \kappa \mathbf{n} \delta(\mathbf{x} - \mathbf{x}_f) dA, \quad (2)$$

where μ_s , ρ , p , \mathbf{u} , and $\boldsymbol{\sigma}$ denote the solvent viscosity and the density of the fluid, the pressure, the velocity vector, and the viscoelastic extra stress tensor, respectively. The last term in Eq. (2) represents the body force due to surface tension, where γ is the surface tension coefficient, κ is twice the mean curvature, and \mathbf{n} is the unit vector normal to the interface. The surface tension acts only on the interface as indicated by the three-dimensional delta function δ , whose arguments \mathbf{x} and \mathbf{x}_f are the points at which the equation is being evaluated and a point at the interface, respectively.

The FENE-CR model [31] is adopted as the constitutive equation for the viscoelastic extra stresses. This model can be written as

$$\begin{aligned} \frac{\partial \mathbf{A}}{\partial t} + \nabla \cdot (\mathbf{u} \mathbf{A}) - (\nabla \mathbf{u})^T \cdot \mathbf{A} - \mathbf{A} \cdot \nabla \mathbf{u} &= -\frac{F_A}{\lambda} (\mathbf{A} - \mathbf{I}), \\ F_A &= \frac{L^2}{L^2 - \text{tr}(\mathbf{A})}, \end{aligned} \quad (3)$$

where \mathbf{A} , λ , L , F_A , and \mathbf{I} are the conformation tensor, the relaxation time, the extensibility parameter defined as the ratio of the length of a fully extended polymer dumbbell to its equilibrium length, the stretch function, and the identity tensor, respectively. The extra stress tensor $\boldsymbol{\sigma}$ is related to the

conformation tensor as

$$\boldsymbol{\sigma} = \frac{F_A \mu_p}{\lambda} (\mathbf{A} - \mathbf{I}), \quad (4)$$

where μ_p is the polymeric viscosity. The amount of polymeric viscosity is controlled by the polymer concentration defined as $c = \frac{\mu_p}{\mu_s}$.

It is also assumed that the material properties remain constant following a fluid particle, i.e.,

$$\frac{D\rho}{Dt} = 0, \quad \frac{D\mu_s}{Dt} = 0, \quad \frac{D\mu_p}{Dt} = 0, \quad \frac{D\lambda}{Dt} = 0, \quad (5)$$

where $\frac{D}{Dt} = \frac{\partial}{\partial t} + \mathbf{u} \cdot \nabla$ is the material derivative. The density, polymeric and solvent viscosities, and the relaxation time vary discontinuously across the fluid interface and are given by

$$\begin{aligned} \mu_p &= \mu_{p,d}\phi + \mu_{p,a}(1-\phi), & \mu_s &= \mu_{s,d}\phi + \mu_{s,a}(1-\phi), \\ \rho &= \rho_d\phi + \rho_a(1-\phi), & \lambda &= \lambda_d\phi + \lambda_a(1-\phi), \end{aligned} \quad (6)$$

where the subscripts d and a denote the properties of the drop and the ambient fluids, respectively. The indicator function ϕ is defined such that it is unity inside the droplet and zero outside.

The flow equations (1) and (2) are solved fully coupled with the viscoelastic model equations (3) by the finite-difference–front-tracking method developed by Izbassarov and Muradoglu [29]. The flow and viscoelastic model equations are solved on a staggered Eulerian grid using a projection method [32]. The log-conformation method of Fattal and Kupferman [33] is employed to enhance numerical stability in solving the viscoelastic model equations at high Weissenberg numbers. A fifth-order upwind WENO-Z [34] scheme is used to discretize the convective terms in the viscoelastic constitutive equations while all the other spatial derivatives are approximated using central differences. Time integration is achieved using a first-order explicit Euler method for both the flow and viscoelastic model equations. Although it is straightforward to make the present numerical method second-order accurate in time, a first-order method is used here since the time-stepping error is generally found to be negligibly small compared to the spatial error mainly due to a small time step imposed by the numerical stability of the present explicit scheme [29].

A separate Lagrangian grid is used to explicitly track the fluid-fluid interface. The Lagrangian grid consists of linked marker points moving with the local flow velocity interpolated from the stationary Eulerian grid. The surface tension is computed on the Lagrangian grid and then distributed onto the Eulerian grid points near the interface and added to the momentum equations as body force [35]. The indicator function is computed at each time step based on the location of the interface using the standard procedure [35] and is then used to set the fluid properties in each phase according to Eq. (6). The Lagrangian grid is restructured at every time step by deleting the front elements that are smaller than a prespecified lower limit and by splitting the front elements that are larger than a prespecified upper limit in the same way as described by Tryggvason *et al.* [35] to keep the front element size nearly uniform and comparable to the Eulerian grid size. A complete description of the front-tracking method can be found in Ref. [35] and the treatment of the viscoelasticity and contact line in Refs. [29,30] and Ref. [28], respectively.

III. PROBLEM STATEMENT

The droplet is initially spherical and is placed near the wall with a uniform impact velocity V_{col} , as shown in Fig. 1. The flow is assumed to be axisymmetric so only one half is used as the computational domain. The computational domain extends five drop radii in both the radial and axial directions. The surrounding air is initially quiescent. The viscosity and density ratios are set to $\rho_d/\rho_a = \mu_d/\mu_a = 20$ in all the results presented here. Note that the density and viscosity ratios are an order of magnitude larger in a typical liquid-air system than those specified here. However, it has been previously demonstrated [6,28,36] that a further increase in the property ratios does not affect

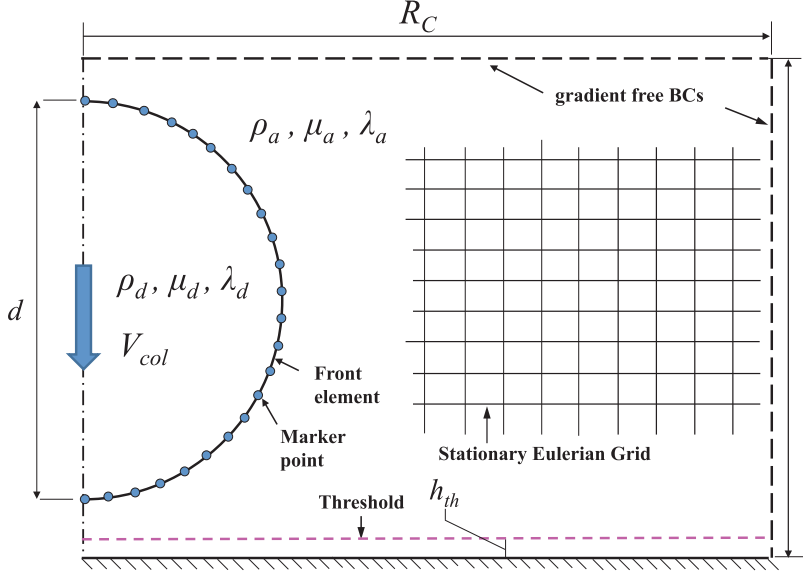


FIG. 1. Schematic illustration of the computational setup. The interface is represented by the connected Lagrangian marker points. The flow and viscoelastic model equations are solved on a uniform Eulerian Cartesian grid. The droplet is initialized near the wall with a spherical shape and uniform collision velocity V_{col} .

the results significantly. Therefore, the property ratios are kept small in order to enhance numerical stability and thus to reduce the computational cost.

The no-slip boundary conditions (BCs) yield a stress singularity near the contact line and so require a special treatment. The slip-contact line model is essentially the same as that of Muradoglu and Tasoglu [28], so it is briefly summarized here. In the framework of the front-tracking method, the drop interface must be connected to the solid wall explicitly. To achieve this, we assume that the drop interface connects to the wall when the distance between the drop interface and solid wall gets shorter than a prespecified threshold value h_{th} (Fig. 1). For this purpose, the interface is monitored and the front element crossing the threshold line is detected. Then this element is connected to the solid wall such that the contact angle between the wall and droplet is equal to the apparent contact angle θ_D . In the present work, the threshold length is typically taken as $h_{th} = 3\Delta x$, where Δx is the Eulerian grid size and the apparent contact angle is specified dynamically using the Kistler correlation [37,38] that relates the apparent contact angle to the capillary number defined as $Ca_{CL} = \mu_d V_{CL}/\gamma$, where V_{CL} is the speed of the contact line. To determine the dynamic contact angle, we first compute

$$\theta_{D_i} = f_{\text{Hoff}}(Ca_{CL} + f_{\text{Hoff}}^{-1}(\theta_e)), \quad (7)$$

where θ_e is the equilibrium (static) contact angle and f_{Hoff}^{-1} is the inverse of the Hoffman function defined as

$$f_{\text{Hoff}}(x) = \arccos \left\{ 1 - 2 \tanh \left[5.16 \left(\frac{x}{1 + 1.31x^{0.99}} \right)^{0.706} \right] \right\}. \quad (8)$$

The dynamic contact angle is then computed in the advancing and receding phases as

$$\theta_D = \begin{cases} \theta_{D_i} & \text{if } V_{CL} \geq 0 \quad (\text{advancing}) \\ 2\theta_e - \theta_{D_i} & \text{if } V_{CL} < 0 \quad (\text{receding}). \end{cases}$$

Following Muradoglu and Tasoglu [28], the contact line velocity V_{CL} is specified as the velocity of the point where the droplet interface crosses the threshold. The details of the implementation of this slip contact line method can be found in Ref. [28].

The governing equations are solved in their dimensional forms and the results are expressed in terms of the relevant dimensionless quantities. The length and velocity scales are defined as an initial drop diameter d and impact velocity V_{col} , respectively, and $T = d/V_{col}$ is the time scale. Then, in addition to the property ratios, the other relevant dimensionless numbers are defined as

$$Wi = \frac{\lambda V_{col}}{d}, \quad We = \frac{\rho_d V_{col}^2 d}{\sigma}, \quad Re = \frac{\rho_d V_{col} d}{\mu_d}, \quad (9)$$

where Wi , We , and Re are the Weissenberg, Weber, and Reynolds numbers, respectively.

IV. RESULTS AND DISCUSSION

Simulations are carried out to study effects of viscoelasticity on drop impact, spreading, and rebound. The computational domain is resolved by a 1024×1024 uniform Cartesian grid in all the results presented in this paper. Since an extensive grid convergence study of the present numerical method has been previously performed by Muradoglu and Tasoglu [28], such a study is not repeated here. However, we checked the grid convergence and ensured that the solutions are grid independent, i.e., the spatial error is below 3% for all the results presented here.

Simulations are first performed to examine the sole effects of the droplet fluid viscoelasticity without the polymer-induced contact angle hysteresis. Then a model is incorporated into the numerical method to mimic the modification of the substrate wettability due to deposition of polymer molecules and further simulations are carried out to test the performance of the model.

A. Simulations without polymer-induced hysteresis

We first designate a base case to systematically examine the effects of various flow parameters. Based on the experimental data [39] as well as the numerical stability and convergence considerations, the base case is defined as $Re = 35$, $We = 30$, $Wi = 1$, $L^2 = 225$, $c = 1.27$, and $\theta_e = 145^\circ$.

The evolution of drop impact and spreading is visually depicted for the base case in Fig. 2, where the velocity vectors and the contours of average polymer extension $\sqrt{\text{tr}(\mathbf{A})}$ are shown on the left- and right-hand sides, respectively. Note that the velocity vectors are plotted at every 35 grid points in both coordinate directions in all the results presented in this paper to better show the flow patterns. The square root of the trace of the conformation tensor $\sqrt{\text{tr}(\mathbf{A})}$ is plotted here as a measure of average polymer length. A smooth interface without any artificial flow near the contact line can be considered as an indication of overall good accuracy of the numerical solution. As can be seen in the figure, the drop spreads in the radial direction after it impacts on the surface. During the spreading phase polymers are extended due to velocity gradients in the direction parallel to the solid wall, resulting in a thin viscoelastic boundary layer, as can be better seen in the enlarged version of the droplets in Fig. 3 at time $t^* = 1.0$ for the $Wi = 1$ and $Wi = 10$ cases. In the boundary layer, the polymers near the interface exert an extensional stress that pushes the contact line to increase the spreading rate. This is the main mechanism that makes the polymer droplets spread more than that of the Newtonian one. At the end of the spreading phase, i.e., at about $t^* = 1.3$, the drop reaches its maximum spreading as the initial impacting kinetic energy is totally exhausted. The initial kinetic energy of the drop is partially dissipated, partially converted to the surface energy, and partially stored as the elastic energy. As the drop reaches its maximum spreading it takes a usual disklike form with a thin central part (often called lamella), surrounded by a circular rim. At this point, the flow changes direction from spreading outward to receding inward. During the receding phase, the rim swells and moves inward until it reaches the axis of symmetry. As the droplet retracts, the viscoelastic stresses concentrate along the axis of symmetry while the stresses near the wall diminish. The stresses along the wall counteract the retraction of the contact line, but this effect decreases

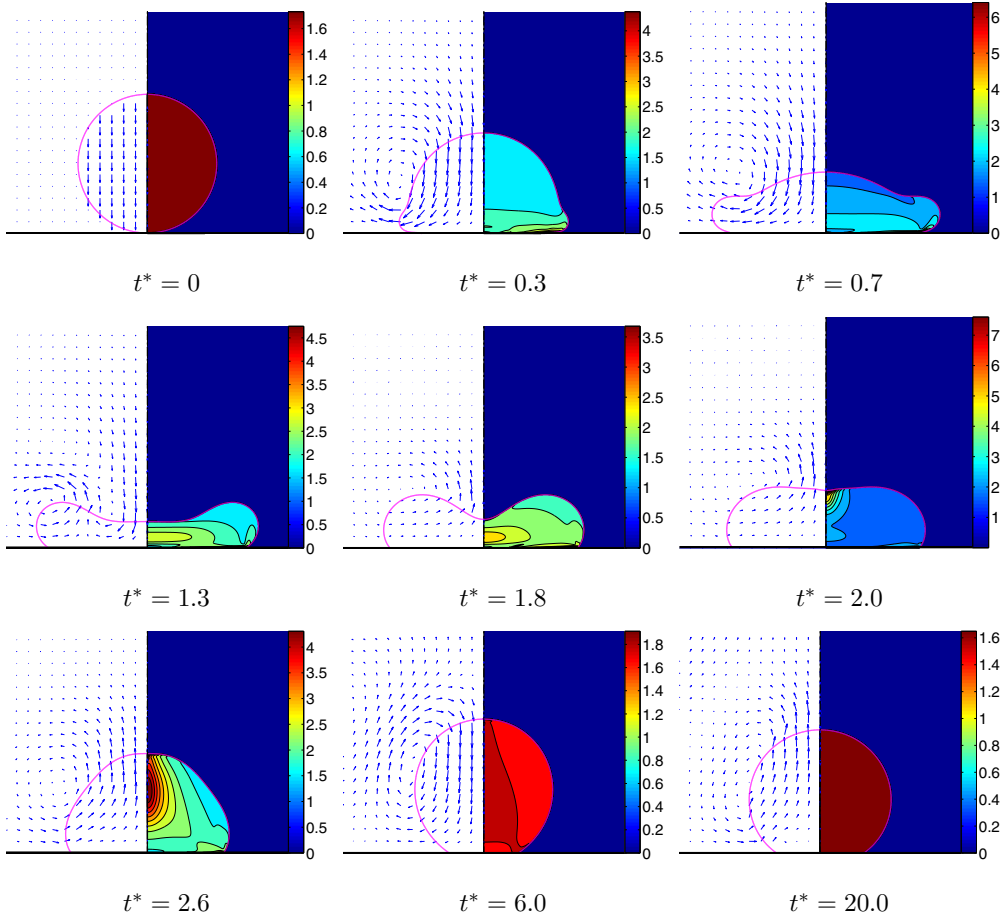


FIG. 2. Evolution of a FENE-CR droplet after impacting on the solid surface. The velocity vectors are plotted on the left and the contours of average polymer extension $\sqrt{\text{tr}(\mathbf{A})}$ on the right. The parameters are $\text{Re} = 35$, $\text{We} = 30$, $\text{Wi} = 1$, $L^2 = 225$, $c = 1.27$, and $\theta_e = 145^\circ$.

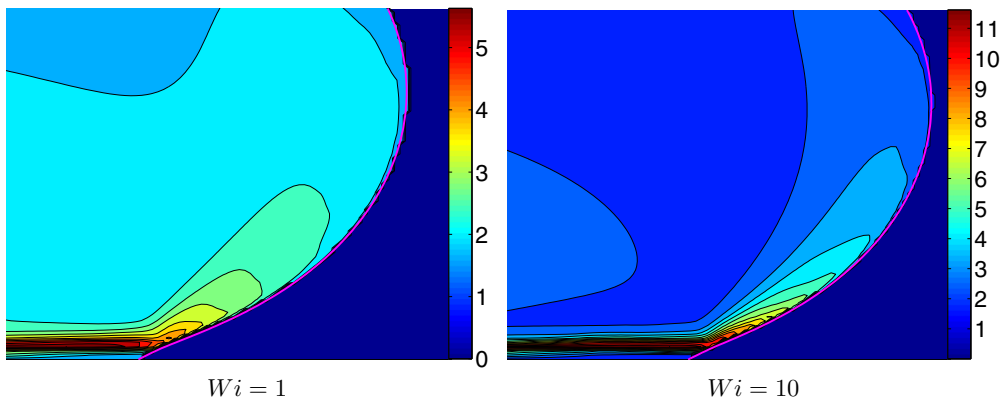


FIG. 3. Contours of average polymer extension $\sqrt{\text{tr}(\mathbf{A})}$ in the vicinity of the contact line for $\text{Wi} = 1$ (left) and $\text{Wi} = 10$ (right). The snapshots are taken at time $t^* = 1$. The other parameters are $\text{Re} = 35$, $\text{We} = 30$, $L^2 = 225$, $c = 1.27$, and $\theta_e = 145^\circ$.

as the polymer molecules relax due to the reversal flow. The same internal flow is also responsible for the stress concentration along the drop centerline near the apex of the droplet. As a result, the stresses along the axis of symmetry force the fluid to flow upward and thus favor drop retraction. Depending on the remaining kinetic energy of the droplet, two different outcomes are possible: The droplet can either oscillate on the surface or rebound. In both cases, the droplet eventually reaches an equilibrium with a spherical cap shape on the substrate.

Next we investigate the effects of the flow parameters on the drop dynamics. For this purpose, simulations are performed to examine the effects of the Weissenberg number by varying Wi in the range $0 \leq Wi \leq 100$ while the other parameters are the same as the base case. The evolution of

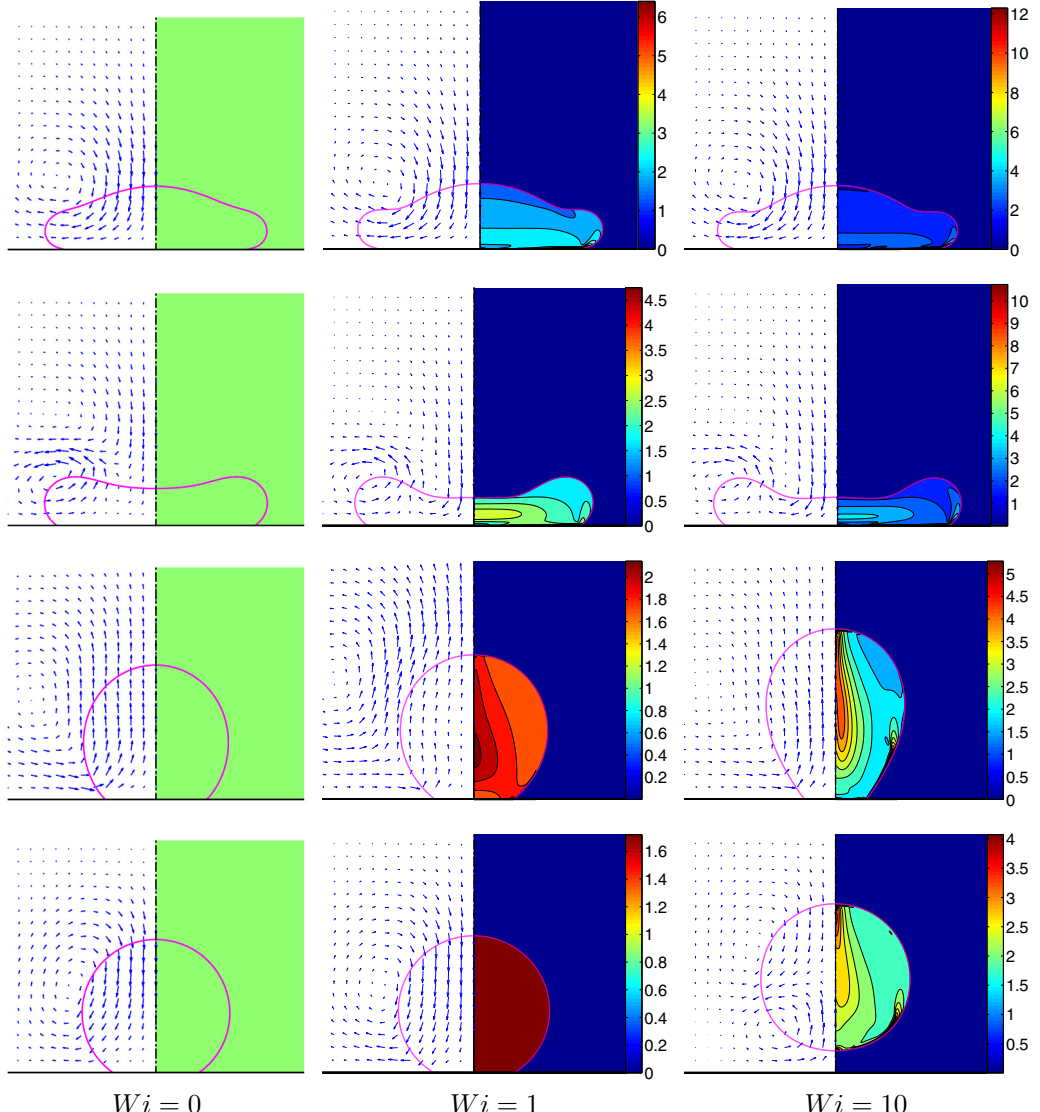


FIG. 4. Effects of Wi on drop impact. The time evolution is from top to bottom. The velocity vectors are plotted on the left and the contours of average polymer extension $\sqrt{\text{tr}(\mathbf{A})}$ on the right. The snapshots are taken at the times $t^* = 0.7, 1.3, 5.0$, and 7.5 . The other parameters are $Re = 35$, $We = 30$, $L^2 = 225$, $c = 1.27$, and $\theta_e = 145^\circ$.

drop shapes are plotted in Fig. 4 for $Wi = 0$ (Newtonian), $Wi = 1$, and $Wi = 10$. As can be seen, the magnitude of the viscoelastic stresses monotonically increases as Wi is increased. However, unlike the Oldroyd-B model, the FENE-CR model bounds the growth of the viscoelastic stresses. Therefore, the increase in the stresses gets smaller when Wi exceeds a threshold value, i.e., when $Wi \geq 10$ in this case. It is interesting to see that the viscoelasticity favors spreading of the droplet and the viscoelastic droplet tends to spread more than that of the Newtonian one, which is in agreement with the computational results of Tomé *et al.* [23] and Fang *et al.* [19]. While there is no significant difference between the $Wi = 1$ and $Wi = 10$ cases in the advancing phase, in the retraction phase, the difference is more pronounced and the retraction becomes faster as Wi increases. When the retraction velocity is fast enough, the fluid rises from the center of droplet forming a dome, which may even result in a complete rebound from the substrate; see, e.g., the $Wi = 10$ case in Fig. 4. As discussed above, part of the initial kinetic energy is stored as elastic energy in the viscoelastic drop, which reduces the energy dissipation in the spreading phase. This elastic energy is then released during the recoiling phase contributing to the drop rebound. This finding is in agreement with the experimental observation of Bertola [9]. The effects of Wi are quantified in Fig. 5, where the spread factor is plotted as a function of nondimensional time. The spread factor is defined as the radius of the wetted spot normalized by the equivalent drop radius. The results obtained for a Newtonian droplet are also plotted in this figure to directly show the effects of the viscoelasticity. The viscosity in the Newtonian case is set to the total viscosity of the corresponding viscoelastic case, i.e., $\mu_{\text{Newtonian}} = \mu_s + \mu_p$. The Weissenberg number seems to have little influence on the spread factor in the spreading phase, but its influence is more pronounced in the receding phase. However, the maximum spread factor slightly increases with Wi (Fig. 5) mainly due to the increased viscoelastic stresses, which favor spreading (Fig. 4). More importantly, the tendency for rebound increases as Wi increases and the drop rebounds when $Wi \geq 4$ in this case.

Obviously, these results are in contrast with the polymeric antirebound phenomenon. Recent studies have revealed that, when the substrate effects are removed, the viscoelasticity in drop fluid reduces the overall energy dissipation and thus increases the tendency of a drop rebound [9]. Our computational results are consistent with these findings and support the hypothesis that the antirebound effect results from the modification of wetting properties of the substrate due to polymer deposition. This issue will be discussed in more detail in Sec. IV B.

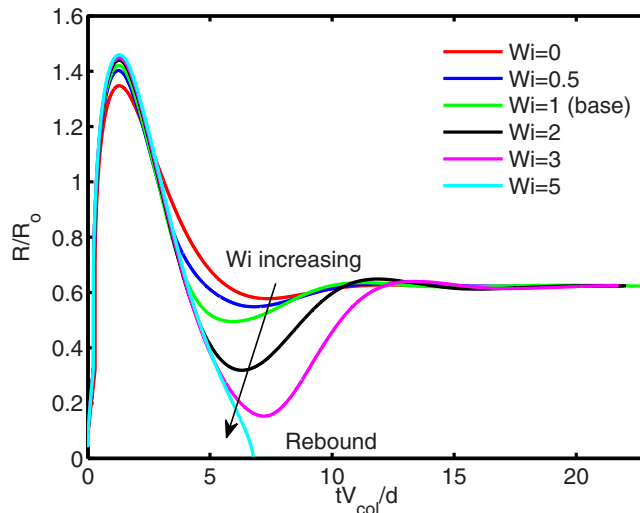


FIG. 5. Effects of the Weissenberg number on droplet impact and spreading. Time evolution of the spread factor is plotted for various values of Wi in the range $0 \leq Wi \leq 5$. The other parameters are $Re = 35$, $We = 30$, $L^2 = 225$, $c = 1.27$, and $\theta_e = 145^\circ$.

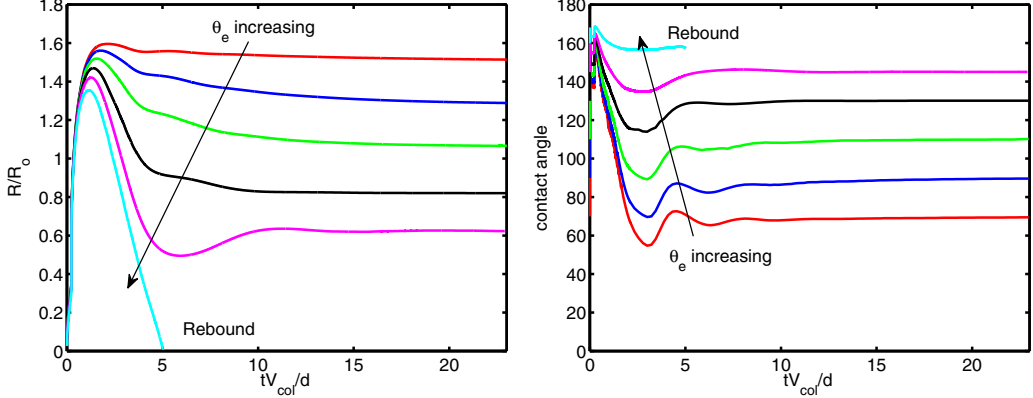


FIG. 6. Effects of the equilibrium contact angle on droplet impact and spreading in the range $70^\circ \leq \theta_e \leq 160^\circ$. The other parameters are $Re = 35$, $We = 30$, $Wi = 1$, $L^2 = 225$, and $c = 1.27$.

Next, computations are performed for a range of equilibrium contact angles varying between 70° and 160° and the results are plotted in Fig. 6. Similar to the Newtonian case [28], the equilibrium contact angle significantly influences the spreading and rebound of the drop. As expected, the tendency to rebound increases as the substrate becomes more hydrophobic. We also performed simulations to examine the effects of the dynamic contact angle in comparison with the fixed static contact angle. This is done because numerical simulations are often performed using a static contact angle in the literature. For this purpose, we simulated a hydrophobic case, i.e., $\theta_e = 150^\circ$, using both the dynamic and static contact angle formulations. The results are shown in Fig. 7. This figure clearly shows a large discrepancy between two formulations: The drop rebounds in the static contact angle case while it undergoes damped oscillations on the substrate in the dynamic contact angle case.

Then we examine the effects of the Weber number on the drop impact and spreading by varying the Weber number between 10 and 1000 while keeping the other parameters the same as the base case. The results are plotted in Fig. 8. Upon impact, the initial kinetic energy is partly stored as surface energy, which is proportional to the maximum spreading diameter. Thus the maximum spread factor increases with the Weber number since the surface tension decreases, making the interface more deformable. The retraction phase is governed by the balance between the surface energy, the

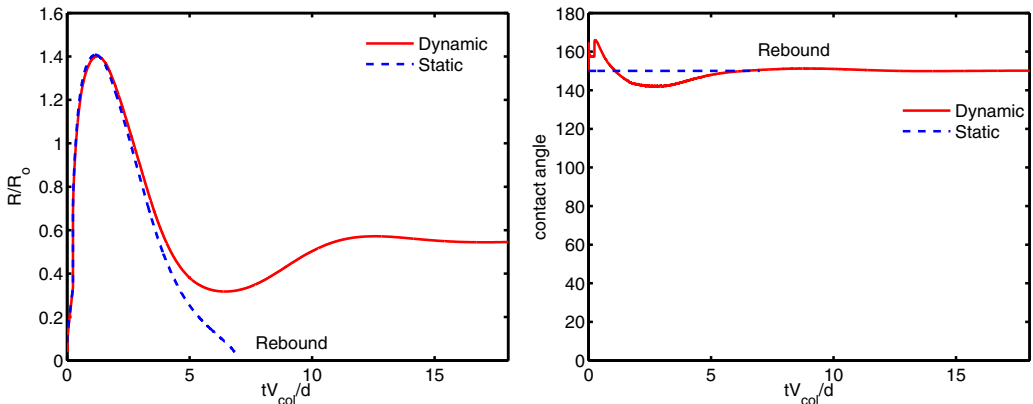


FIG. 7. Effects of the static and dynamic contact angles on droplet impact and spreading. The parameters are $Re = 35$, $We = 30$, $Wi = 1$, $L^2 = 225$, $c = 1.27$, and $\theta_e = 150^\circ$.

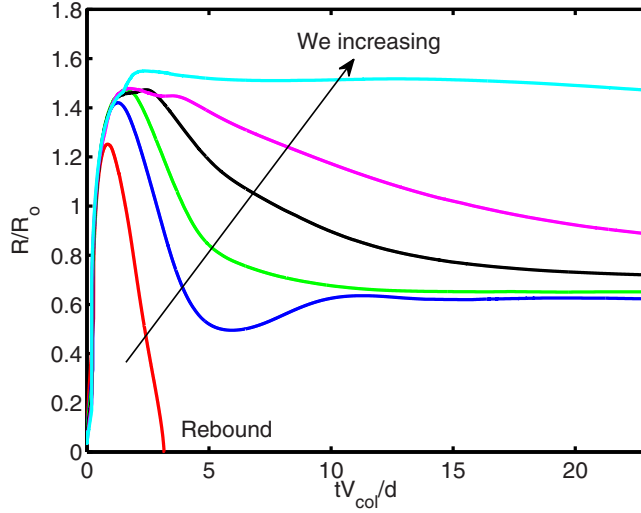


FIG. 8. Effects of the Weber number. The evolution of spread factor is plotted for $We = 10, 30, 50, 100, 200$, and 1000 . The other parameters are $Re = 35$, $Wi = 1$, $L^2 = 225$, $c = 1.27$, and $\theta_e = 145^\circ$.

viscous dissipation, and elastic energy stored in the polymers. As the Weber number decreases, more energy is stored as surface energy to be released during the receding phase and thus the droplet retracts faster. For the same reason, as We decreases, the droplet shifts to a rebound regime after a critical value, i.e., $We_{cr} \sim 20$ in this case. It is also observed that the viscoelastic effects are more pronounced at lower Weber numbers. For instance, the droplet rebounds in the case of $We = 20$ and $Wi = 1$ for which the Newtonian counterpart sticks to the substrate as shown in Fig. 9.

The Reynolds number is an important parameter that measures the relative significance of the inertial forces compared to the viscous forces. The effects of the Reynolds number are examined for both the Newtonian and viscoelastic droplet cases and the results are shown in Fig. 10, where

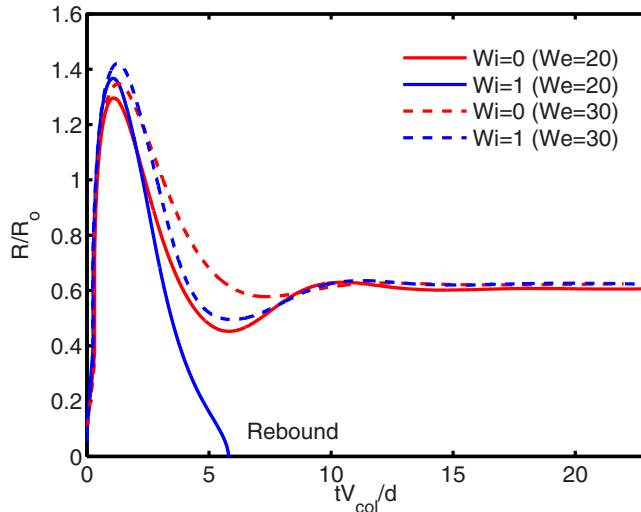


FIG. 9. Effects of the Weber number on the impact and spreading of a Newtonian $Wi = 0$ and a viscoelastic $Wi = 1$ droplet. The solid and dashed lines denote the results obtained for $We = 20$ and $We = 30$, respectively. The other parameters are $Re = 35$, $L^2 = 225$, $c = 1.27$, and $\theta_e = 145^\circ$.

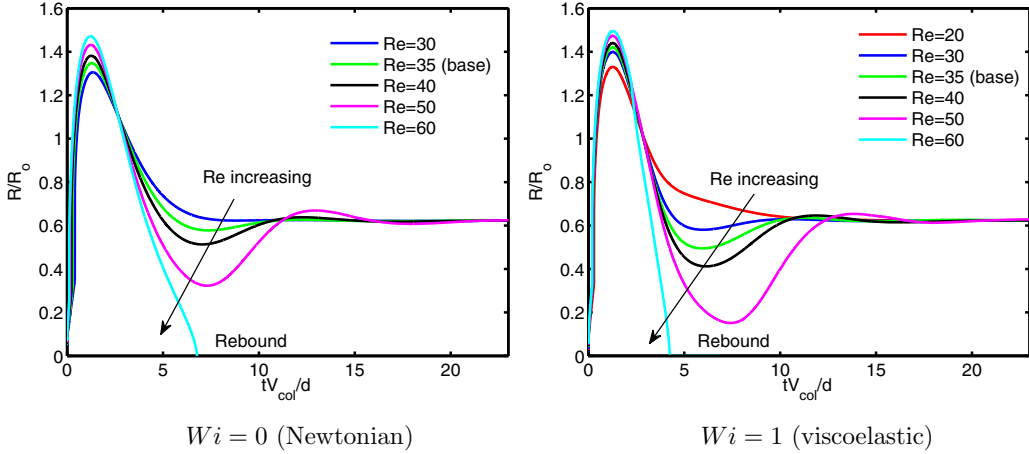


FIG. 10. Effects of the Reynolds number for a Newtonian (left) and a viscoelastic (right) droplet in the range $\text{Re} = 20\text{--}60$. The other parameters are $\text{We} = 30$, $L^2 = 225$, $c = 1.27$, and $\theta_e = 145^\circ$.

the spread factor is plotted as a function of the nondimensional time for various Reynolds numbers ranging between $\text{Re} = 20$ and 60. This figure shows that the maximum spreading rate and the tendency of drop rebound increase with Re for both the Newtonian and viscoelastic drop cases. This is expected since the viscous dissipation is reduced as Re increases and thus more energy is left to be first stored as surface energy and then released during the receding phase. It is also observed that the viscoelasticity enhances both the maximum spread factor and the tendency of drop rebound since part of the initial kinetic energy is stored as elastic energy in the polymers. This elastic energy is released during the receding phase, contributing to the drop kinetic energy.

In a typical experimental study, the fluid viscoelasticity is increased by adding more polymers to the same solvent fluid. In this way, the polymeric viscosity changes while the solvent viscosity remains essentially unchanged. To mimic this, we performed simulations for a range of polymeric viscosities while keeping the other rheological properties fixed in the base case. In fact, not only the polymeric viscosity, but also the relaxation time changes as more polymers are added to the solvent. Here we take the advantage of the computational simulations to examine the sole effects of the polymeric viscosity. The results are shown in Fig. 11(a), where the evolution of the spread factor is plotted for $c = 0, 0.5, 0.75, 1$, and 1.27. The concentration appears to have a large influence on the spread factor especially in the receding phase. As c increases, both the maximum spread factor and the tendency for rebound decrease. Even though these results seem to be consistent with the antirebound phenomenon, it is mainly caused by the additional viscous dissipation rather than the viscoelastic effects. To verify this, further simulations are also performed for the corresponding Newtonian cases by setting the viscosity to the total viscosity of the viscoelastic counterpart, i.e., $\mu_{\text{Newtonian}} = \mu_s + \mu_p$. The results are shown in Fig. 11(b). As can be seen, decreasing Reynolds number has an effect similar to increasing concentration factor. Nevertheless, a close examination of the viscoelastic and Newtonian cases in Fig. 11 reveals that the viscoelasticity favors drop rebound opposed to the experimental observations [8].

B. Effects of polymer-induced hysteresis

The experimental studies have revealed that there is a substantial hysteresis in the contact angle in the advancing and receding phases [8]. This hysteresis is believed to be related to the deposition of the polymer molecules on the substrate during the advancing phase [16]. Smith and Bertola [12] observed that the deposited polymers outside the drop are stretched during the receding phase, which in turn slows down the movement of the contact line. This mechanism can be interpreted as a dissipative force or an effective friction force acting in the direction opposite the contact line,

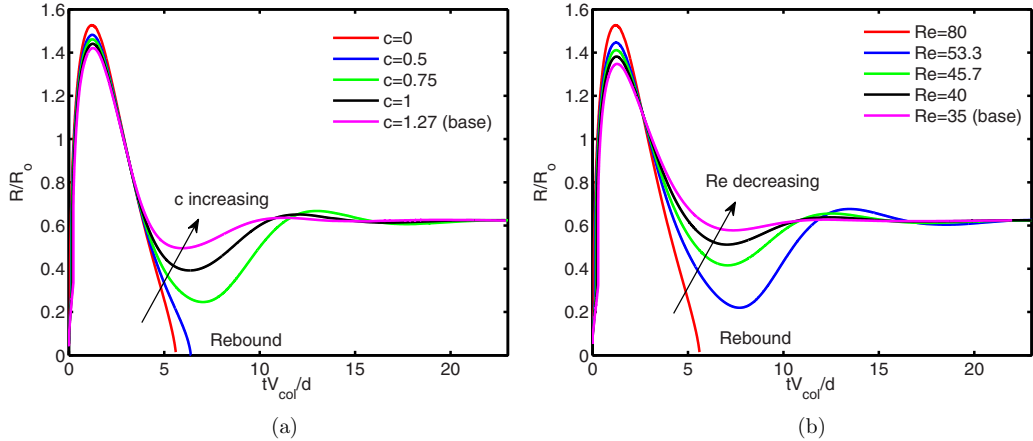


FIG. 11. (a) Effects of the polymer concentration on the droplet impact and spreading compared to (b) the corresponding Newtonian cases. The evolution of the spread factor is shown for (a) $c = 0, 0.5, 0.75, 1.0$, and 1.27 and $Wi = 1$ in the viscoelastic case corresponding to (b) $Re = 80, 53.3, 45.7, 40$, and 35 and $Wi = 0$ in the Newtonian case. The other parameters are $We = 30$, $L^2 = 225$, and $\theta_e = 145^\circ$.

leading to a reduction in dynamic contact angle during the receding phase. Bertola and Wang [16] have recently shown that the contact angle may exhibit an underdamped or overdamped oscillatory behavior depending on the flow condition. However, the contact angle decays nearly exponentially during the first receding phase in both cases. To mimic this behavior, we propose a simple model for the polymer-induced hysteresis and modify the equilibrium contact angle θ_e as

$$\theta_e = \begin{cases} \theta_c & \text{in the first advancing period} \\ \theta_s + (\theta_c - \theta_s)e^{-t_e/T_d} & \text{otherwise,} \end{cases} \quad (10)$$

where t_e , T_d , θ_c , and θ_s are the exposure time, the deposition time scale, and the clean and saturated equilibrium contact angles, respectively. The exposure time is defined as the total time that the part of the substrate has been wetted by the drop fluid. The deposition time scale characterizes how fast the substrate wettability is modified by the polymers and is an empirical parameter that can be found from fitting the model to the experimental data. The hysteresis effect reduces as T_d

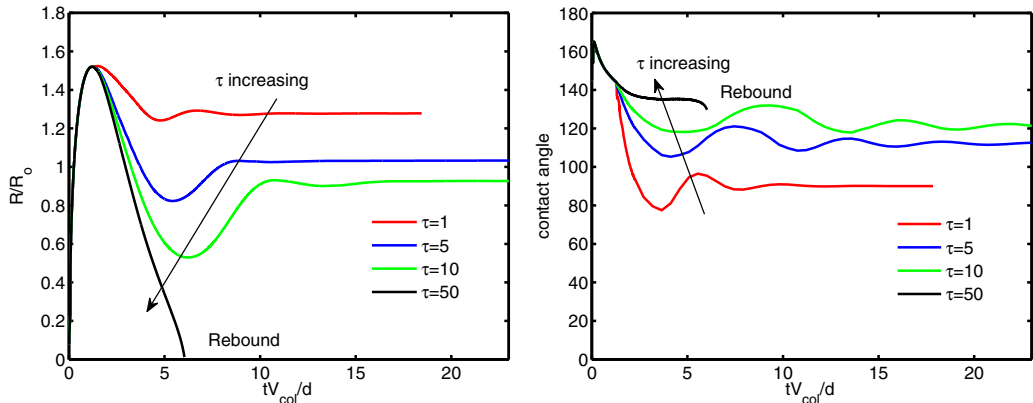


FIG. 12. Effects of the nondimensional deposition time scale τ on the droplet impact and spreading in the range $1 \leq \tau \leq 50$. The other parameters are $Re = 75$, $We = 30$, $Wi = 1$, $L^2 = 225$, $c = 0.075$, $\theta_c = 145^\circ$, and $\theta_s = 90^\circ$.

increases and no-hysteresis conditions are recovered in the limit as $T_d \rightarrow \infty$. Note that this lumped model incorporates all the unknown physics that are responsible for the antirebound effect into an empirical parameter T_d rather than fully characterizing the realistic physical mechanism, which is left for future study.

To test the performance of this model, we slightly modify the base case so that the drop rebound occurs in the absence of the polymer-induced hysteresis. Thus the new base case is designated as $\text{Re} = 75$, $\text{We} = 30$, $\text{Wi} = 1$, $L^2 = 225$, $c = 0.075$, $\theta_c = 145^\circ$, and $\theta_s = 90^\circ$. Note that the drop rebounds for this set of the parameters if $\theta_s = \theta_c$ as shown in Fig. 10.

Simulations are first carried out to examine the effects of the deposition time scale and the results are shown in Fig. 12, where the evolution of the spread factor and the dynamic contact angle is plotted for various values of the nondimensional deposition time scale defined as $\tau = T_d V_{\text{col}}/d$ in the range $1 \leq \tau \leq 50$. As can be seen, the drop rebound is suppressed as τ is reduced, which qualitatively shows good agreement with the antirebound effect of polymer additives observed in the experimental studies. Note that the maximum spread factor is essentially unaffected by τ since the hysteresis is switched on at the beginning of the receding phase. This is also consistent with the experimental results of Bertola and Wang [16]. Further simulations are performed to examine the effects of the saturated equilibrium contact angle θ_s on drop dynamics and the results are shown in Fig. 13 for $\tau = 1$ and 10. The drop rebound is again suppressed as θ_s decreases. Moreover, the dynamic contact angle oscillates in a fashion similar to the experimental results of Bertola and

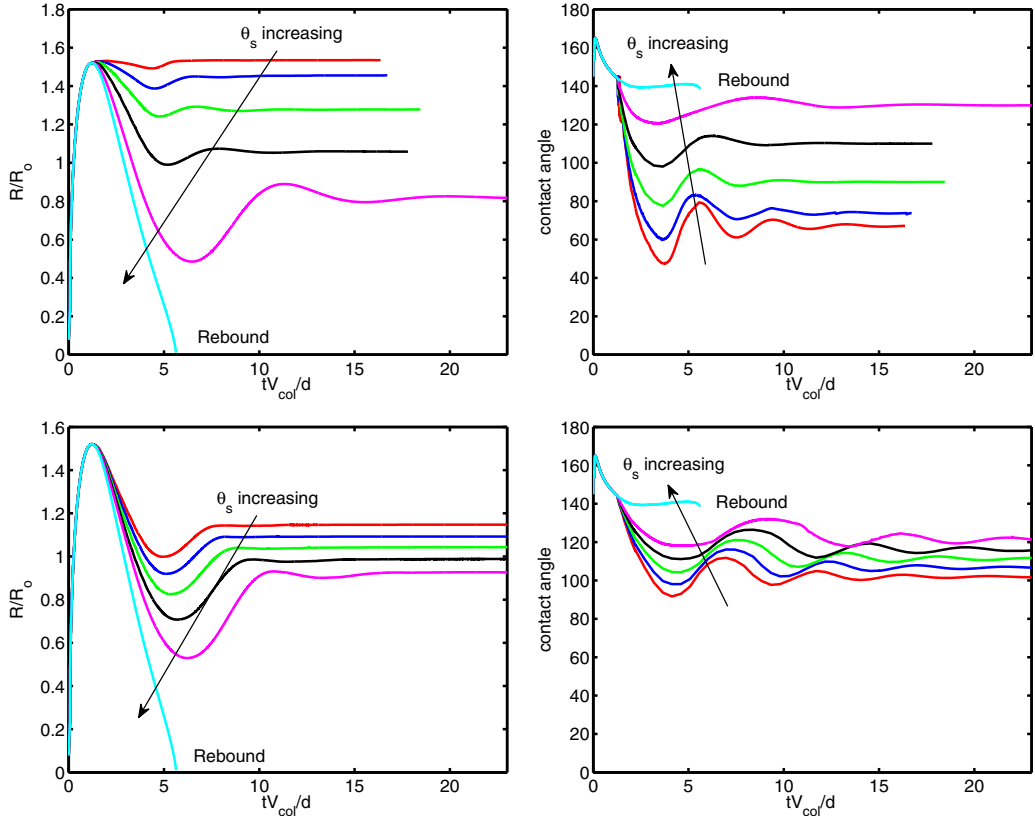


FIG. 13. Effects of the saturated equilibrium contact angle θ_s on the drop impact and spreading for the fast deposition $\tau = 1$ in the range $50 \leq \theta_s \leq 145$ (top row) and the slow deposition $\tau = 10$ in the range $10 \leq \theta_s \leq 145$ (bottom row). The other parameters are $\text{Re} = 75$, $\text{We} = 30$, $\text{Wi} = 1$, $L^2 = 225$, $c = 0.075$, and $\theta_c = 145^\circ$.

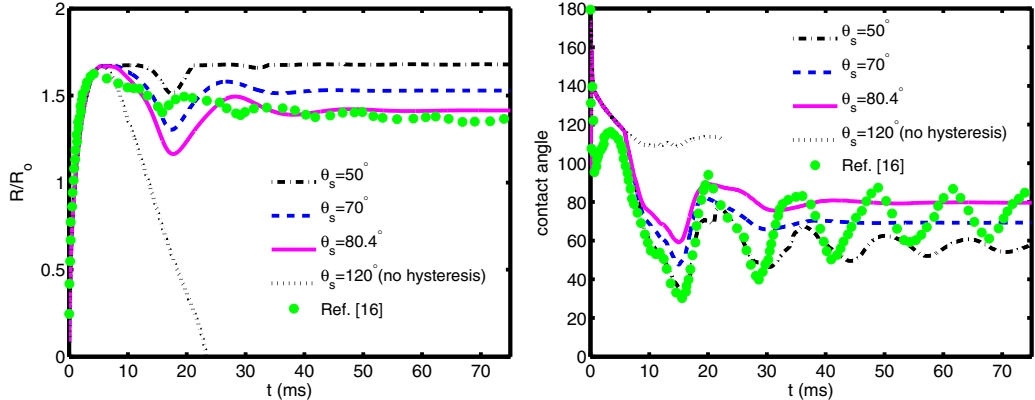


FIG. 14. Effects of the saturated equilibrium contact angle θ_s on PEO drop impact and spreading on a PTFE surface for $\tau = 0.5$ in the range $50^\circ \leq \theta_s \leq 120^\circ$. The other parameters are $Re = 200$, $We = 15$, $Wi = 5.92$, $L^2 = 225$, $c = 0.23$, and $\theta_c = 120^\circ$.

Wang [16], especially for $\tau = 10$ (Fig. 13). These results support that the antirebound effect is mainly due to the modification of the surface wetting properties by the deposited polymer molecules rather than the bulk fluid properties, which is in agreement with the experimental observations of Bertola [8], Bertola and Wang [16], and Huh *et al.* [18].

Finally, the performance of the model is quantified by directly comparing the computational results with the experimental data of Bertola and Wang [16], i.e., polyethylene oxide (PEO) drop impacting and spreading on a polytetrafluoroethylene (PTFE) surface. In the simulations, the material properties of the polymeric solution are set to its physical values, except for the extensibility parameter L , which was not specified by Bertola and Wang [16]. Thus we set $L^2 = 225$ as in the base case. Note that, although not shown here, our numerical simulations show that the effects of L on drop impact dynamics are negligibly small in the range of $5 \leq L < \infty$. Moreover, the Reynolds number is taken here as an order of magnitude lower than that in the experimental study mainly for the numerical reasons, i.e., the convergence rate of the pressure solver starts deteriorating significantly after $Re > 200$ and becomes prohibitively slow when $Re > 300$. Thus we set $Re = 200$ in the present study. The Weber number, the Weissenberg number, the polymer concentration, and the equilibrium contact angle are the same as in the experiment, i.e., $We = 15$, $Wi = 5.92$, $c = 0.23$, and $\theta_c = 120^\circ$. The saturated equilibrium contact angle is deduced from the experimental spread factor as $\theta_s = 80.4^\circ$ by assuming that the droplet has a spherical cap shape at the latest time reported by Bertola and Wang [16]. Simulations are performed for the various saturated contact angles in the range $50^\circ \leq \theta_s \leq 120^\circ$ to show the sensitivity of the computational results to θ_s . Note that $\theta_s = 120^\circ$ corresponds to the no-hysteresis case. The results are compared with the experimental data in Fig. 14. As can be seen in this figure, $\theta_s = 80.4^\circ$ yields reasonably good agreement with the experimental data for the spread factor, especially in the later times. However, the oscillatory behavior of the contact angle is better captured for the lower values, i.e., for $\theta_s = 50^\circ$. We note that it is not clear exactly where the contact angle is measured in the experiments. In addition, there is about $\pm 10\%$ measurement error in the experimental data [16].

V. CONCLUSION

The effects of viscoelasticity on the drop impact, spreading, and rebound on a solid surface were studied computationally using a front-tracking method. The FENE-CR model was employed to account for the viscoelasticity of drop fluid. Extensive simulations were performed to examine the effects of the fluid elasticity characterized by the Weissenberg number Wi and the polymer

concentration c as well as the equilibrium contact angle θ_e , the Reynolds Re, and the Weber We numbers.

When the polymer-induced hysteresis effects were ignored, we found that the maximum spread factor is enhanced slightly by the viscoelasticity, which is in agreement with the experimental and the numerical results reported in the literature. However, in contrast with the well-known antirebound effect of the polymer additives, the viscoelasticity was found to favor drop rebound. These effects are pronounced as Wi is increased. The equilibrium contact angle and the Weber and Reynolds numbers were found to have similar effects for both the Newtonian and viscoelastic cases: The tendency of a drop rebound strongly depends on and increases with the equilibrium contact angle and decreases with the Weber number. Similarly, the drop rebound is favored when the Reynolds number increases. The effects of viscoelasticity were found to be more pronounced at low Weber and high Reynolds numbers. Simulations were also performed to examine the effects of the dynamic contact angle on the drop dynamics. As in the Newtonian case [28], the dynamic contact angle was found to be crucially important for accurate prediction of drop spreading and rebound. Further simulations were carried out to examine the effects of polymer concentration by changing the polymeric viscosity while keeping the solvent viscosity unchanged. It was found that the drop rebound is suppressed as the polymeric viscosity is increased mainly due to the enhanced viscous dissipation.

Finally, the effects of polymer-induced hysteresis were examined. For this purpose, a simple model was developed to mimic the hysteresis due to deposition of polymer molecules on the substrate. It was found that the model is able to predict the antirebound effect of the polymeric additives and the results were found to be in reasonably good agreement with the experimental observations. The present results provide further evidence that the antirebound effect of polymer additives is related to the modification of the surface wetting properties rather than the drop fluid elasticity.

ACKNOWLEDGMENTS

This work was supported by the Scientific and Technical Research Council of Turkey, Grant No. 112M181, and by the European network action COST MP1106 “Smart and green interfaces-from single bubbles and drops to industrial, environmental and biomedical applications.”

- [1] V. Bergeron, D. Bonn, J. Y. Martin, and L. Vovelle, Controlling droplet deposition with polymer additives, *Nature (London)* **405**, 772 (2000).
- [2] S. D. Aziz and S. Chandra, Impact, recoil and splashing of molten metal droplets, *Int. J. Heat Mass Transfer* **43**, 2841 (2000).
- [3] Y. Son and C. Kim, Spreading of inkjet droplet of non-Newtonian fluid on solid surface with controlled contact angle at low Weber and Reynolds numbers, *J. Non-Newtonian Fluid Mech.* **162**, 78 (2009).
- [4] A. L. Yarin, Drop impact dynamics: Splashing, spreading, receding, bouncing, *Annu. Rev. Fluid Mech.* **38**, 159 (2006).
- [5] U. Demirci and G. Montesano, Single cell epitaxy by acoustic picolitre droplets, *Lab Chip* **7**, 1139 (2007).
- [6] S. Tasoglu, G. Kaynak, A. J. Szeri, U. Demirci, and M. Muradoglu, Impact of a compound droplet on a flat surface: A model for single cell epitaxy, *Phys. Fluids* **22**, 082103 (2010).
- [7] R. Rioboo, M. Marengo, and C. Tropea, Time evolution of liquid drop impact onto solid, dry surfaces, *Exp. Fluids* **33**, 112 (2002).
- [8] V. Bertola, Dynamic wetting of dilute polymer solutions: The case of impacting droplets, *Adv. Colloid Interface Sci.* **193-194**, 1 (2013).
- [9] V. Bertola, An experimental study of bouncing Leidenfrost drops: Comparison between Newtonian and viscoelastic liquids, *Int. J. Heat Mass Transfer* **52**, 1786 (2009).

- [10] A. Rozhkov, B. Prunet-Foch, and M. Vignes-Adler, Impact of drops of polymer solutions on small targets, *Phys. Fluids* **15**, 2006 (2003).
- [11] D. Bartolo, A. Boudaoud, G. Narcy, and D. Bonn, Dynamics of Non-Newtonian Droplets, *Phys. Rev. Lett.* **99**, 174502 (2007).
- [12] M. I. Smith and V. Bertola, Effect of Polymer Additives on the Wetting of Impacting Droplets, *Phys. Rev. Lett.* **104**, 154502 (2010).
- [13] D. Y. Zang, X. L. Wang, X. G. Geng, Y. J. Zhang, and Y. M. Chen, Impact dynamics of droplets with silica nanoparticles and polymer additives, *Soft Matter* **9**, 394 (2013).
- [14] D. Y. Zang, W. X. Zhang, J. Y. Song, Z. Chen, Y. J. Zhang, X. G. Geng, and F. Chen, Rejuvenated bouncing of non-Newtonian droplet via nanoparticle enwrapping, *Appl. Phys. Lett.* **105**, 231603 (2014).
- [15] M. I. Smith and J. S. Sharp, Origin of contact line forces during the retraction of dilute polymer solution drops, *Langmuir* **30**, 5455 (2014).
- [16] V. Bertola and M. Wang, Dynamic contact angle of dilute polymer solution drops impacting on a hydrophobic surface, *Colloids Surf. A* **481**, 600 (2015).
- [17] D. Biolè and V. Bertola, The role of the microscale contact line dynamics in the wetting behaviour of complex fluids, *Arch. Mech.* **67**, 401 (2015).
- [18] H. K. Huh, S. Jung, K. W. Seo, and S. J. Lee, Role of polymer concentration and molecular weight on the rebounding behaviors of polymer solution droplet impacting on hydrophobic surfaces, *Microfluid. Nanofluid.* **18**, 1221 (2015).
- [19] J. Fang, R. G. Owens, L. Tacher, and A. Parriaux, A numerical study of the SPH method for simulating transient viscoelastic free surface flows, *J. Non-Newtonian Fluid Mech.* **139**, 68 (2006).
- [20] T. Jiang, J. Ouyang, B. Yang, and J. Ren, The SPH method for simulating a viscoelastic drop impact and spreading on an inclined plate, *Comput. Mech.* **45**, 573 (2010).
- [21] T. Jiang, J. Ouyang, L. Zhang, and X. Li, Improved SPH approach to branched polymer free surface flows based on the XPP model, *Polym. Plast. Technol. Eng.* **50**, 203 (2011).
- [22] T. Jiang, L.-G. Lu, and W.-G. Lu, The numerical investigation of spreading process of two viscoelastic droplets impact problem by using an improved SPH scheme, *Comput. Mech.* **53**, 977 (2014).
- [23] M. Tomé, N. Mangiavacchi, J. A. Cuminato, A. Castelo, and S. McKee, A finite difference technique for simulating unsteady viscoelastic free surface flows, *J. Non-Newtonian Fluid Mech.* **106**, 61 (2002).
- [24] C. M. Oishi, F. P. Martins, M. F. Tomé, and M. A. Alves, Numerical simulation of drop impact and jet buckling problems using the eXtended Pom-Pom model, *J. Non-Newtonian Fluid Mech.* **169-170**, 91 (2012).
- [25] G. S. Paulo, C. M. Oishi, M. F. Tomé, M. A. Alves, and F. T. Pinho, Numerical solution of the FENE-CR model in the complex flows, *J. Non-Newtonian Fluid Mech.* **204**, 50 (2014).
- [26] Y. Wang, D. Q. Minh, and G. Amberg, Dynamic wetting of viscoelastic droplets, *Phys. Rev. E* **92**, 043002 (2015).
- [27] S. O. Unverdi and G. Tryggvason, A front-tracking method for viscous, incompressible, multi-fluid flows, *J. Comput. Phys.* **100**, 25 (1992).
- [28] M. Muradoglu and S. Tasoglu, A front-tracking method for computational modeling of impact and spreading of viscous droplets on solid walls, *Comput. Fluids* **39**, 615 (2010).
- [29] D. Izbassarov and M. Muradoglu, A front-tracking method for computational modeling of viscoelastic two-phase systems, *J. Non-Newtonian Fluid Mech.* **223**, 122 (2015).
- [30] D. Izbassarov and M. Muradoglu, A computational study of two-phase viscoelastic systems in a capillary tube with a sudden contraction/expansion, *Phys. Fluids* **28**, 012110 (2016).
- [31] M. D. Chilcott and J. M. Rallison, Creeping flow of dilute polymer-solutions past cylinders and spheres, *J. Non-Newtonian Fluid Mech.* **29**, 381 (1988).
- [32] A. R. Chorin, Numerical solution of the Navier-Stokes equations, *Math. Comput.* **22**, 745 (1968).
- [33] R. Fattal and R. Kupferman, Time-dependent simulation of viscoelastic flows at high Weissenberg number using the log-conformation representation, *J. Non-Newtonian Fluid Mech.* **126**, 23 (2005).
- [34] R. Borges, M. Carmona, B. Costa, and W. S. Don, An improved weighted essentially non-oscillatory scheme for hyperbolic conservation laws, *J. Comput. Phys.* **227**, 3191 (2008).

- [35] G. Tryggvason, B. Bunner, A. Esmaeeli, D. Juric, N. Al-Rawahi, W. Tauber, J. Han, S. Nas, and Y.-J. Jan, A front-tracking method for the computations of multiphase flow, *J. Comput. Phys.* **169**, 708 (2001).
- [36] U. Olgac, D. Izbassarov, and M. Muradoglu, Direct numerical simulation of an oscillating droplet in partial contact with a substrate, *Comput. Fluids* **77**, 152 (2013).
- [37] S. F. Kistler, in *Wettability*, edited by J. C. Berg (Dekker, New York, 1993), pp. 311–429.
- [38] Š. Šikalo, H.-D. Wilhelm, I. V. Roisman, S. Jakirlić, and C. Tropea, Dynamic contact angle of spreading droplets: Experiments and simulations, *Phys. Fluids* **17**, 062103 (2005).
- [39] M. Tembely, D. Vadillo, M. R. Mackley, and A. Soucemarianadin, The matching of a “one-dimensional” numerical simulation and experiment results for low viscosity Newtonian and non-Newtonian fluids during fast filament stretching and subsequent break-up, *J. Rheol.* **56**, 159 (2012).